Atomic structure and composition of the 2 × N reconstruction of the Ge wetting layer on Si(001) investigated by surface x-ray diffraction

T. Zhou,[1] G. Renaud,[1] C. Revenant,[1] J. Issartel,[1] T. U. Schülli,[1] R. Felici,[2] and A. Malachias[2]
[1]*CEA, Institut Nanosciences et Cryogénie, SP2M, NRS, F-38054 Grenoble, France*
[2]*ESRF, Boite Postale 220, F-38043 Grenoble, France*
(Received 21 May 2010; revised manuscript received 7 March 2011; published 17 May 2011)

The $2 \times N$ reconstruction of the Ge/Si(001) wetting layer has been investigated by surface x-ray diffraction. At a substrate temperature of 670 °C, the average N periodicity decreases from $N = 11.5$ to 8 with an increasing Ge coverage from one to three monolayers (ML). The top layer consists of asymmetric dimers with a bond length in the range of 2.50–2.60 Å and a buckling angle in the range of 9.4°–15.6°, depending on the Ge coverage. The obtained dimer bond lengths are similar to those calculated for alternating asymmetric mixed dimers. Intermixing of Ge with Si is found down to the sixth (eighth) layer for 2 (from 3 to 5) ML coverage. For 2 ML coverage, a quantitative surface x-ray diffraction data set has been measured. It is analyzed using a model describing the atomic structure and Ge occupation probability with a limited set of parameters to bypass the intrinsic lack of appreciable reflections of the $2 \times N$ ($N = 9$) reconstruction. The Ge occupation probability varies periodically along the N direction, having its minimum value below the dimer vacancy lines. In addition, a more direct calculation of the Lorentz and detector acceptance corrections is given for rocking and radial scans.

DOI: 10.1103/PhysRevB.83.195426 PACS number(s): 68.35.B−, 68.47.Fg, 61.05.cp

I. INTRODUCTION

Ge islands on Si(001) have been studied extensively because of their novel electronic and optical properties related to quantum confinement.[1] Apart from its relevance to applications, the heteroepitaxy of Ge on Si has become a prototype system for the investigation of the Stranski-Krastanow growth mode. Because of an identical crystal structure and atomic bonding but a 4.2% mismatch in lattice parameter, Ge first forms a wetting layer (WL) before islands start to nucleate for Ge deposits larger than four monolayers (ML). Island structure, nucleation,[2] ripening,[3] facet evolution,[4,5] and alloying[6] have been studied intensively, and many of the underlying mechanisms are now reasonably understood. However, less attention has been paid to the structure and composition of the WL, despite the fact that they are intimately linked to the growth of the Ge islands. The process of island nucleation on the WL cannot just be described by the capture of newly deposited Ge atoms, since it also involves a diffusive interaction with the WL.[7] At growth temperatures around 600 °C, a substantial amount of material is transferred from the WL to the islands during the initial stages of their formation.[8] Thus, a quantitative determination of the WL structure and composition is essential for a better understanding of island formation and intermixing.

The top layer of the Ge WL on Si(001) is composed of dimers, as are the clean, 2×1 reconstructed Si(001) and Ge(001) surfaces. The structure and symmetry of these dimers have been the object of quite a few studies. X-ray standing waves[9] and high-resolution photoemission concluded to the dimer asymmetry, i.e., dimers with two atoms at different heights. Moreover, mixed Si-Ge asymmetric dimers were found at the beginning of the growth; Ge occupying the up site and Si the down site.[10] A first-principles molecular cluster total-energy and atomic-force calculation confirmed that asymmetric dimers are energetically more stable than symmetric ones, thanks to a charge transfer from down to up dimer atoms.[11] Photoelectron diffraction studies further suggested that the buckling angle of a mixed dimer is significantly larger than that of a pure Si dimer.[12] A theoretical study confirmed that buckling of Si-Ge dimers is energetically favorable, Si (Ge) occupying the down (up) site. The higher buckling angle for these dimers is also confirmed by theory.[13] It was also shown that, as in the cases of 2×1 reconstructed Si and Ge (001) surfaces, the uppermost Ge layer can be composed of alternating asymmetric dimer structures, where in-phase or out-of-phase buckling of adjacent dimer rows leads to $p(2 \times 2)$ or $c(4 \times 2)$ reconstructions, respectively.[14] Theoretical calculations further predicted that alternating asymmetric dimers correspond to the most stable structure for Ge/Si(001).[15] A room-temperature (RT) scanning tunneling microscopy (STM) study of the Ge(001) surface showed that, within a single substrate dimer row, neighboring dimers buckle in opposite directions.[16] Atom-tracking STM showed that mixed dimers are highly buckled and appear to "rock" between two configuration states with 180° rotational symmetry.[17,18]

The lattice mismatch is partially accommodated in the WL by removing every Nth line of dimers: the WL is characterized by a $(2 \times N)$ reconstruction[19] consisting of a periodic arrangement of dimer vacancy lines (DVLs) of the (2×1) dimer reconstruction. The value of N results from a balance between the energy gain from strain relief and the energy cost of forming dimer vacancies. N varies with the WL thickness, and depends on the Si-Ge intermixing, which is another mechanism for strain relief. Intermixing in the WL was confirmed by several experimental means: X-ray photoelectron diffraction and Auger electron diffraction,[20] transmission electron microscopy, Raman spectroscopy and photoluminescence,[21] and high-resolution Rutherford backscattering spectroscopy.[22] For example, this last study yielded Ge concentrations in the first four layers to be 64.5%, 38%, 22.5%, and 11% for 1.5 ML of Ge deposited at 500 °C. Besides these experiments, intermixing was also studied theoretically. A Monte Carlo (MC) simulation showed that, for 1 ML coverage, entropy

counteracts the wetting nature of Ge and mixes the two top layers. As an example, at a deposition temperature of 677 °C and 1.2 ML coverage (with enough Ge to completely coat the surface), 14% of the surface atoms were found to be Si.[23] In the same study, the occupation probabilities of Ge in the first four layers were calculated as a function of Ge coverage. For 2 ML, the Ge concentration of the second layer was found to be only 1/3 at 600 °C. Another MC simulation concluded to a site selectivity of intermixing, mainly induced by the dimer rows and DVLs.[24] The DVLs induce atomic displacements in their vicinity, corresponding to a local compressive strain. Hence, the surrounding of the DVLs is unfavorable for larger atoms, and in this case, Ge.[24]

When the Ge coverage exceeds the value corresponding to the minimal equilibrium dimer vacancy separation, the stress cannot be further relieved by additional dimer vacancies. The additional stress relaxation is achieved by forming dimer-row vacancies (DRVs) every M dimer rows. The resulting structure is called a patched structure or $M \times N$ reconstruction.[25,26] Because DRVs are less efficient than the DVLs in relieving the strain, M decreases faster than N with increasing coverage. The state of the art of the Ge/Si(001) WL reveals a fragmented knowledge of the Ge/Si(001) $2 \times N$ (and $M \times N$) reconstruction. To the best of our knowledge, no precise experimental determination of the WL structure exists, nor does that of the in-depth displacements and composition below the surface. The present study aims at determining the structure and composition of the $2 \times N$ reconstruction, with special attention to the dimer configuration and the predicted site selectivity.

The $2 \times N$ reconstruction has been investigated by surface x-ray diffraction (SXRD),[27] which is a powerful technique to determine the atomic positions, as well as the intermixing, at a surface and within a few layers below, with high sensitivity during growth at a chosen substrate temperature, in an ultrahigh-vacuum (UHV) environment. The SXRD experimental setups are described in Sec. II. The value of the deposition temperature (670 °C) was chosen to favor a possible atomic order in the WL. As a matter of fact, zones of atomic order were claimed to exist in Ge/Si(001) domes grown in this temperature range.[28] In Sec. III, general characteristics of the reconstruction are presented, such as the size of the reconstructed domains and terraces, the N periodicity, and intermixing. Then, the 2×1 reconstruction of 1, 2, and 3 ML coverage is studied, followed by the $2 \times N$ reconstruction at 2 ML coverage. In Sec. IV, the discussion deals with the configuration of the buckling dimers, the N periodicity, the atomic displacements, intermixing, and the site selectivity of Si and Ge. Finally, the Appendix presents calculations of specific corrections (Lorentz, detector acceptance) that are mandatory to correctly evaluate the integrated intensities of the $\times N$ diffraction rods.

II. SXRD EXPERIMENTS

The experiments were carried out at two surface diffraction beamlines at the European Synchrotron Radiation Facility (ESRF). The first measurements, in which only the $\times 2$ diffraction rods were measured, were performed at the BM32[29] bending magnet beamline for 0, 1, 2, and 3 ML Ge deposits at 670 °C. The $\times N$ reconstruction data were recorded in a second run at the ID03[30] undulator beamline, for 2 ML Ge coverage at 670 °C. Both beamlines are equipped with a z-axis type diffractometer, holding a heavy-duty UHV chamber equipped with beryllium windows to let the x-ray beam enter and exit the chamber. In both cases, the x-ray energy was set to 11 keV and the openings of the detector slit (located 570 mm from the sample center) were set to 2 mm in both directions, parallel and perpendicular to the sample surface. A standard scintillation detector was used. The incident angle was equal to the critical angle (0.163°) for total external reflection of Si at this energy. At BM32, the doubly focused incident x-ray beam size was 0.3×0.3 mm^2 ($H \times V$); it had a divergence of 1×0.1 mrad^2 ($H \times V$). At ID03, the beam was doubly focused to a size of 0.05×0.1 mm^2 ($H \times V$), with a divergence of 0.1×0.01 mrad^2 ($H \times V$).

In both cases, the base vacuum was below 1×10^{-10} mbar. The Si(001) surface was deoxidized by heating up to 930 °C for 30 min under a very low flux (<0.1 Å/min) of silicon, resulting in a nice, carbide-free, Si(001)-(2×1) reconstruction as checked by reflection high-energy electron diffraction (RHEED) (at BM32) and grazing incidence x-ray diffraction.

Ge was deposited by molecular beam epitaxy using a Knudsen cell (fluxes of 0.5 Å/min on BM32 and 0.4 Å/min on ID03) monolayer (1.412 Å) after monolayer at 670 °C. The sample growth temperature was measured with a calibrated pyrometer. The measurements were performed at RT.

Since the $\times 2$ reconstruction rods were narrow enough to be integrated along the slit directions, they were measured by rocking scans of the sample around its surface normal, then integrated before standard monitor, area, polarization, and Lorentz corrections were applied.[31,32] Because the $\times N$ rods were too large to be fully integrated by the detector slits, they were all measured through two perpendicular scans: radial and rocking. Specific Lorentz and detector acceptance corrections had to be calculated, as shown in the Appendix. Radial and rocking measurements yielded very close structure factor amplitudes after corrections, thus validating the calculations and measurements (cf. the Appendix).

A real-space lattice is chosen with respect to the conventional fcc lattice. The surface lattice vectors $\mathbf{a}_s$ (x direction) and $\mathbf{b}_s$ (y direction) are parallel to the direction of the dimer ([1$\bar{1}$0]direction) and of the dimer rows ([110] direction), respectively (Fig. 1).

The basis vectors of the unreconstructed (1×1) surface unit cell are

$$\mathbf{a}_s = \left[\frac{1}{2}\frac{\bar{1}}{2}0\right], \quad \mathbf{b}_s = \left[\frac{1}{2}\frac{1}{2}0\right], \quad \mathbf{c}_s = [001], \tag{1}$$

$$\text{with lengths} \quad |\mathbf{a}_s| = \frac{1}{\sqrt{2}}a_0, \quad |\mathbf{b}_s| = \frac{1}{\sqrt{2}}a_0, \quad |\mathbf{c}_s| = a_0,$$

where a_0 is the silicon bulk lattice constant (0.5431 nm).

For the surface unit cell of the 2×1 reconstruction, $\mathbf{a}_s$ is replaced by $\mathbf{a}_s^{2\times 1} = 2 \times \mathbf{a}_s$. For the $2 \times N$ reconstruction,

$$\mathbf{a}_s^{2\times N} = 2 \times \mathbf{a}_s, \quad \mathbf{b}_s^{2\times N} = N \times \mathbf{b}_s, \quad \mathbf{c}_s^{2\times N} = \mathbf{c}_s, \tag{2}$$

$$\text{with} \quad \left|\mathbf{a}_s^{2\times N}\right| = \sqrt{2}a_0, \quad \left|\mathbf{b}_s^{2\times N}\right| = \frac{N}{\sqrt{2}}a_0, \quad \left|\mathbf{c}_s^{2\times N}\right| = a_0.$$

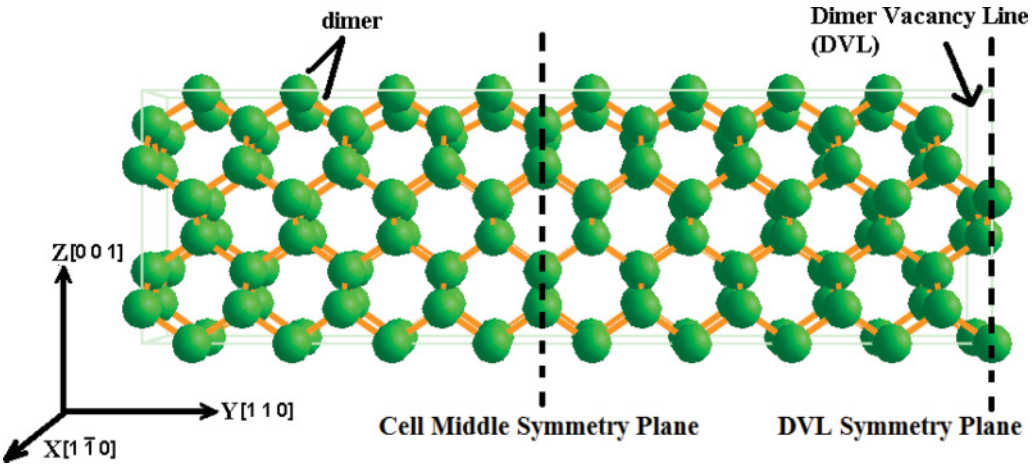

FIG. 1. (Color online) 2 × 9 reconstruction cell for 2 ML Ge/Si(001). There are two symmetry planes parallel to the (*xz*) plane, the cell middle symmetry plane, and the DVL symmetry plane.

For example, a 2 × 9 reconstruction has a surface lattice cell of dimensions 7.681 × 34.563 Å^2. Unless otherwise specified (index "*b*" when the bulk fcc unit cell is used), the (*h*,*k*) reciprocal space units are given in reduced lattice units of the (1×1) or (2×1) surface unit cell.

III. RESULTS

A. General characteristics of the reconstruction

First, the average sizes of terraces and reconstructed domains are evaluated. The reconstruction rods and crystal truncation rods (CTRs) give access to the average size *D* of the reconstructed domains and terraces, respectively, according to

$$D = \frac{2\pi}{\Delta Q_t} \text{ with } \Delta Q_t = Q_{\parallel} \cdot \Delta\omega, \tag{3}$$

where $Q_{\parallel}$ is the in-plane component of the momentum transfer and $\Delta\omega$ is the angular full width at half maximum (FWHM) of the peak situated at **Q** in reciprocal space measured with an in-plane rocking scan.[33] The FWHM of the rocking scans [Figs. 2(a) and 2(b)] of the 2 × 1 reconstruction rods of the clean Si(001) surface are ∼1.64 × 10^{-3} Å^{-1}, which yields an average size of the reconstruction domains of ∼0.38 μm. The $(110)_b$ peak in Fig. 2(c) is the superposition of a 2 × 1 reconstruction rod and a more intense CTR, whose FWHM (4.28 × 10^{-4} Å^{-1}) yields an average terrace size of ∼1.5 μm. Hence, a terrace includes approximately four 2 × 1 reconstructed domains on average. For comparison, the coherence length of the x-ray beam is determined to be ∼3.6 μm at BM32 (from the FWHM of the Si Bragg peak).

Figure 3 shows *h* scans along the $(hh0)_b$ direction for clean Si and for increasing Ge coverage. Due to the crystal symmetry of the diamond lattice, the unit cell is rotated by 90° on two adjacent terraces separated by a monatomic step. Hence, peaks

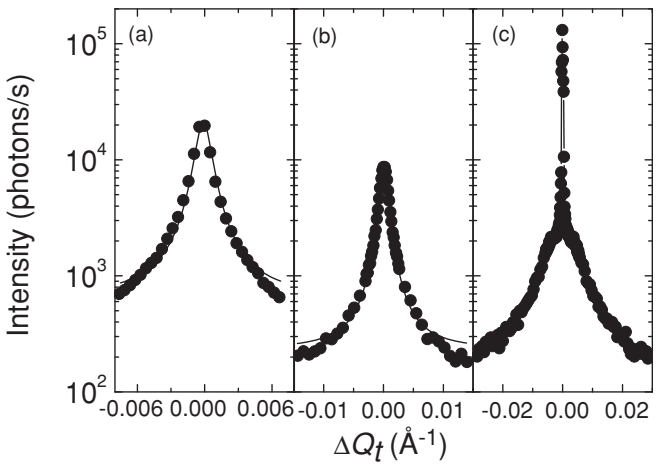

FIG. 2. Some rocking scans of the Si(001)-(2×1) reconstruction (a) $(0.5,0.5,0)_b$, (b) $(1.5,1.5,0)_b$, and (c) $(1\ 1\ 0)_b$, in which a CTR is also present. The lines are Lorentzian fits through the experimental data.

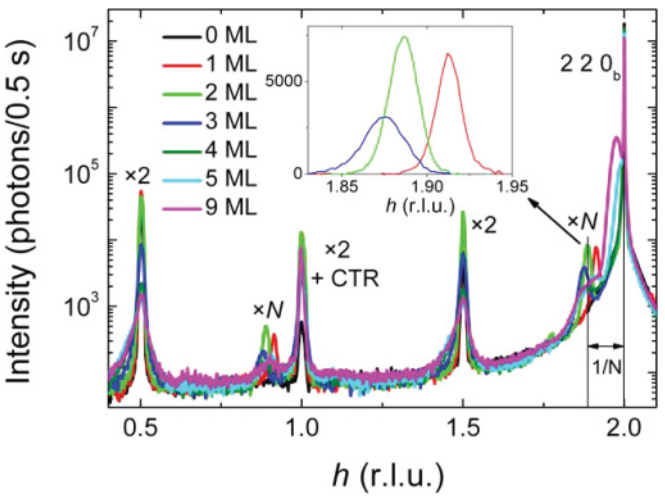

FIG. 3. (Color online) Measured intensity (logarithmic units) at BM32 during radial scans along the $(hh0)_b$ direction for clean Si-(2×1) and for increasing Ge coverage. The separation between the $(220)_b$ peak and its closest ×*N* reconstruction peak, for example, is equal to 1/*N*. The ×*N* reconstruction peaks are much wider and less intense than those of the ×2 reconstruction. Inset: background-subtracted ×*N* rods for 1 (right), 2 (middle), and 3 (left) ML coverage.

from the $\times 2$ and $\times N$ reconstructions can be found on the same h scans. The Si surface is characterized by the $(220)_b$ Bragg peak and $\times 2$ reconstruction peaks: $(0.5,0.5,0)_b$, $(110)_b$, $(1.5,1.5,0)_b$, and $(220)_b$. As soon as the first ML is deposited, a satellite peak of the $(110)_b$ [$(220)_b$] peak appears. This satellite is characteristic of the periodic DVLs with a separation from the main peak inversely proportional to N and is present up to a coverage of at least 9 ML. With an increasing coverage up to 4 ML, this satellite shifts farther away from the $(110)_b$ [$(220)_b$] peak, revealing a decrease of the N periodicity from 11.5 for 1 ML to 9 for 2 ML and to 8 for 3 ML. This satellite (displayed at h slightly smaller than 2 in the inset of Fig. 3) is symmetric and becomes wider with increasing Ge coverage. Its Δh FWHM of 0.016 ± 0.001 for 1 ML, 0.020 ± 0.001 for 2 ML, and 0.029 ± 0.001 for 3 ML yields the size $D = (a_0/\sqrt{2})/\Delta h$ of the $\times N$ reconstructed domain in the in-plane $(hh0)_b$ direction. The D size is 240 ± 15 Å for 1 ML, 192 ± 10 Å for 2 ML, and 132 ± 5 Å for 3 ML. Hence, the domains of the $\times N$ reconstruction are small and become even smaller with increasing Ge coverage. Above 5 ML coverage, the satellite peaks broaden due to an additional contribution from the $\times M$ periodicity. In addition, a shoulder appears on the left side of the Bragg peak, corresponding to the formation of strained islands in the very early stages of the nucleation. At 9 ML coverage, the shoulder moves toward smaller h, indicating a strain relief in larger islands. Remarkably, the $(M \times N)$ reconstruction still exists during the island growth, implying that the WL is still reconstructed in between islands. However, the reconstruction is not as well ordered above 4 ML, once 3D islands have nucleated.

Figure 4 shows h scans along the $(h,h,0.5)_b$ direction, i.e., with a nonzero out-of-plane momentum transfer ($Q_z = 2\pi\ell/c_s$, $\ell = 0.5$) for clean Si and for increasing Ge coverage. This scan is more sensitive to the reconstruction peaks than the in-plane scan thanks to a much lower thermal diffuse scattering background. At 4 ML coverage, the $\times N$ reconstruction peak is less intense and wider than those for smaller Ge deposition. This confirms the presence of a substantial amount of disorder in the $\times N$ reconstruction once islands are formed on the WL.

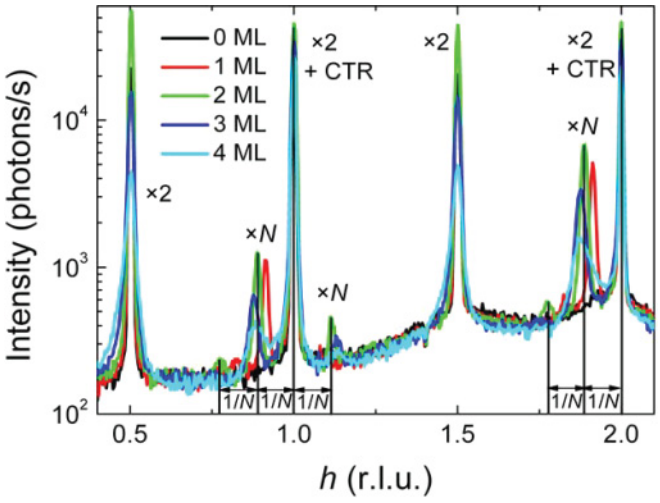

FIG. 4. (Color online) Measured intensity (logarithmic units) at BM32 during radial scans along the $(h,h,0.5)_b$ direction for clean Si and for increasing Ge coverage.

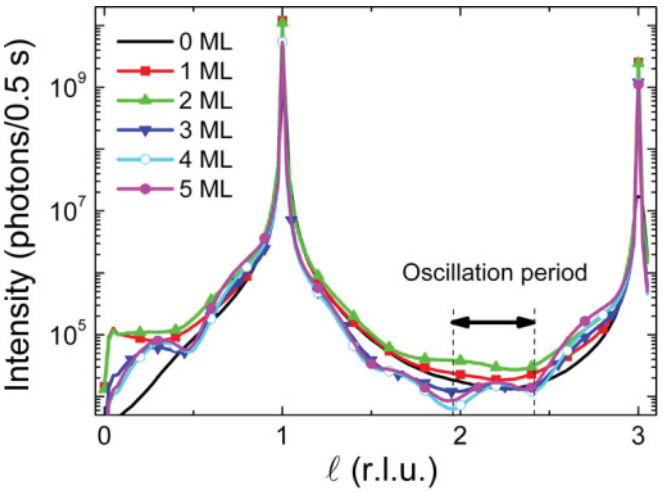

FIG. 5. (Color online) Measured intensity on BM32 (logarithmic units, uncorrected, and not integrated) during a scan along the $(11\ell)_b$ direction for clean Si and increasing Ge coverage.

Figure 5 shows ℓ scans along the $(11\ell)_b$ direction from 0 to 5 Ge ML coverage. The oscillation period observed on the CTR can be used for a rough estimate of the reconstruction depth.[27] For 2 ML coverage, the reconstruction depth is approximately six layers. From 3 to 5 ML coverage, the oscillation period decreases and the reconstruction depth increases to approximately eight layers. No clear oscillations are visible for 1 ML coverage, implying that the reconstruction does not affect the substrate in depth.

In short, the transitions $2 \times 1 \rightarrow 2 \times N$ ($N \sim 11.5$–8) $\rightarrow$ $2 \times 8 + M \times N$ ($M \leqslant 11$) + islands have been identified from 0 to 9 ML coverage. The $\times N$ reconstruction domains are found to be much smaller than those of the $\times 2$ reconstruction.

B. 2 × 1 reconstruction of 1, 2, and 3 ML Ge/Si(001)

1. Model presentation

The aim of this section is to determine the structure and the composition of the 1, 2, and 3 ML Ge/Si(001) WL. In a first step, only the data collected at BM32 are used, and the dimer vacancy lines (the $\times N$ reconstruction) are neglected. Because only the $\times 2$ data are analyzed, the positions and compositions along the y direction are in fact averaged. A surface structure model is refined on the SXRD data. The model has eight layers, which corresponds to the maximum of the reconstruction depth (see Sec. III A). Each layer consists of two atoms that can be displaced along the $[1\bar{1}0]$ and [001] directions. Thus, a complete model comprises 32 displacements. To limit the number of parameters, the model is reduced to only 20 displacements as shown in Fig. 6, similar to the disordered model of Torrelles *et al.*[34] The horizontal atomic displacements in layers (3), (4), (7), and (8) are assumed to be zero, and, in the fifth and sixth layers, the horizontal displacements, as well as the vertical ones, are assumed to be equal within each layer. A vertical symmetry axis is assumed from the third to the eighth layer. The Debye-Waller (DW) factor of the dimer layer is taken anisotropic, i.e., split into in-plane and out-of-plane parameters. The other DW factors are taken isotropic. For the clean Si surface, five independent DW parameters are used

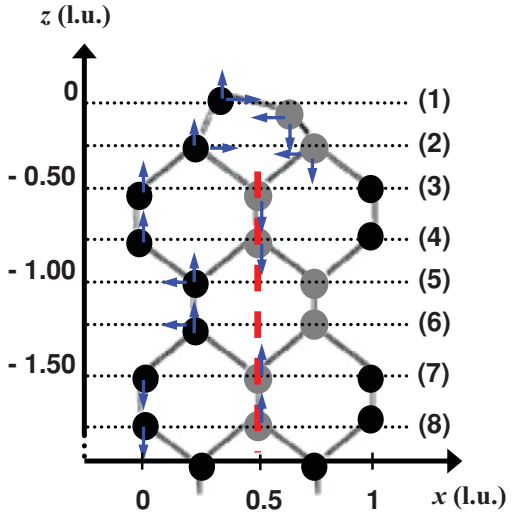

FIG. 6. (Color online) Schematic representation of the atomic positions in the top eight layers. The arrows indicate the displacements of the atoms from their bulk positions (not to scale). The dashed line represents the vertical symmetry axis. In each atomic layer, the black (gray) atom is identified by b (g) in Table I.

to account for the different vibration amplitudes of the dimer layer and the layers below. For the Ge/Si(001) WL, the DW parameters are fixed. For the dimer layer, they are taken equal to those obtained by Torrelles *et al.*[34] for a pure Ge surface, while for the next sublayers, they are fixed to those obtained from the fit of the clean Si(001)-(2 × 1) surface. This simplified model will be validated *a posteriori*.

Because different terraces separated by monatomic steps are present with a 90° rotation of the dimers, two surface structures with equal probability are introduced, namely the above-described one as well as a second one deduced from the first by a 90° rotation plus a $c_s/4$ shift along z [cf. Fig. 7(a)]. As the coherence length of the x-ray beam is close to the terrace size, the waves scattered by up and down terraces are considered to add incoherently.

In addition, the other orientation of the dimer tilt is taken into account by duplicating the above procedures and applying an additional 180° rotation [cf. Fig. 7(b)]. As STM studies showed couplings of Si(001) dimers within a row and also between rows,[35] similar dimer couplings probably exist also for the Ge/Si(001) WL. Hence, the structure factors corresponding to both tilts in the same terrace are added coherently. Each tilt orientation has 1/2 probability.

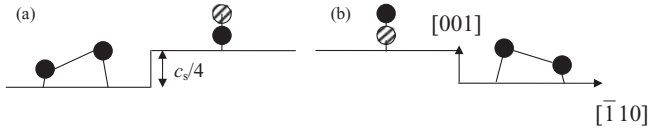

FIG. 7. Schematic representation of the dimer orientation. Up and down adjacent terraces are shifted by $c_s/4$ in the direction normal to the surface. They are equally occupied and are supposed to scatter incoherently. The hatched atoms are at the back. The dimers in (b) correspond to those in (a) rotated by 180°.

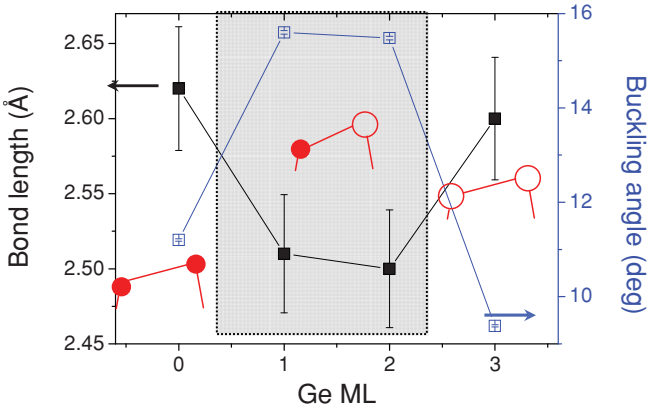

FIG. 8. (Color online) Dimer bond length (filled squares) and buckling angle (open squares) as a function of the Ge coverage. The dimers are represented in three different regimes. The small filled (large open) circles represent the Si (Ge) atoms. The differences in bond lengths and buckling angles are schematic.

2. *Best-fit results*

For each deposition, i.e., Si(001) and 1, 2, and 3 ML Ge/Si(001), six reconstruction rods and six CTRs were measured at BM32 up to an out-of-plane momentum transfer of 3.47 Å^{-1} ($\ell = 3$) with a step size of 0.1 Å^{-1}, totaling 312 independent structure factors. The structure refinement was performed with an adapted version of the ROD software for surface x-ray crystallography,[36] with a χ^2 minimization using the Levenberg-Marquardt method.[37]

The fit of the well-known Si(001)-(2 × 1) reconstruction is first discussed to validate the model. There are in all 27 free parameters (20 displacements, 5 DW parameters, a scale factor, and a fraction of crystal that is covered by the surface layer). This yields a reasonable factor of approximately 11 points per parameter. The best fit leads to $\chi^2 = 1.05$. The corresponding displacement values (listed in Table I) are in good agreement with reported SXRD results on Si(001).[38,39] The bond length and the buckling angle of the dimers are deduced from these displacements (cf. Fig. 8).

The results obtained for the Si(001) surface are satisfactory (as will be shown below) and will serve as the starting point for studying the Ge/Si(001) WL, beginning with a study of its atomic structure along the ×2 (dimer) direction (i.e., averaging over the ×N reconstruction direction).

For the Ge/Si(001) WL, a Ge occupation probability is included in the first four layers for 1 ML and in the first eight layers for 2 and 3 ML. Hence, there are 26 (30) free parameters for 1 (2 and 3) ML (20 displacements, a scale factor, a fraction of covered crystal, and Ge occupation probabilities). This yields a reasonable factor of approximately 12 (10) structure factors per parameter for 1 (2 and 3) ML. The best fit leads to $\chi^2 = 1.3$ for 1 ML, 2.30 for 2 ML, and 2.05 for 3 ML. To illustrate the fit quality, the measured structure factors of reconstruction rods and CTRs are plotted for 1 and 3 ML coverage in Figs. 9(a) and 9(b). The displacements for the best-fit model are listed in Table I. For 1 ML coverage, the displacement values are close to those for clean Si. The Ge occupation probabilities are plotted in Fig. 10. To take into account the DVL, a $1-1/N$ correction is applied to the

TABLE I. Displacement values in Ångströms for the best fit for clean Si-(2×1) (0 ML) and 1, 2, and 3 ML Ge/Si(001)-(2×1). The atomic layer number refers to Fig. 6. For each atomic layer, the atoms are identified by "*b*" (black color in Fig. 6) or "*g*" (gray color in Fig. 6).

Direction	Atomic layer number	Atoms	0 ML	1 ML	2 ML	3 ML
	1	*b*	0.407 ± 0.015	0.530	0.492	0.315
		g	−0.860 ± 0.015	−0.891	−0.937	−0.960
	2	*b*	0.046 ± 0.023	0.123	0.046	0.092
		g	−0.177 ± 0.015	−0.092	−0.038	−0.077
	3	*b*	0	0	0	0
		g	0	0	0	0
	4	*b*	0	0	0	0
		g	0	0	0	0
x	5	*b*	−0.046 ± 0.008	−0.046	−0.038	−0.038
		g	0.046 ± 0.008	0.046	0.038	0.038
	6	*b*	−0.031 ± 0.008	−0.046	−0.046	−0.023
		g	0.031 ± 0.008	0.046	0.046	0.023
	7	*b*	0	0	0	0
		g	0	0	0	0
	8	*b*	0	0	0	0
		g	0	0	0	0
z	1	*b*	0.081 ± 0.027	0.206	0.005	0.234
		g	−0.429 ± 0.038	−0.467	−0.663	−0.19
	2	*b*	0.163 ± 0.022	0.31	0.125	0.282
		g	−0.250 ± 0.027	−0.081	0.13	0.239
	3	*b*	0.054 ± 0.016	0.038	−0.038	0.147
		g	−0.076 ± 0.016	−0.103	−0.152	−0.011
	4	*b*	0.054 ± 0.011	0.125	0.071	0.168
		g	−0.092 ± 0.016	−0.076	−0.06	0.054
	5	*b*	−0.016 ± 0.011	−0.011	−0.027	0.049
		g	−0.016 ± 0.011	−0.011	−0.027	0.049
	6	*b*	0.005 ± 0.011	0.005	0.005	0.06
		g	0.005 ± 0.011	0.005	0.005	0.06
	7	*b*	−0.043 ± 0.011	−0.043	−0.065	−0.005
		g	0.005 ± 0.011	0.027	−0.038	0.054
	8	*b*	−0.005 ± 0.011	−0.022	−0.049	−0.011
		g	0.033 ± 0.011	0.022	−0.016	0.016

occupancy in the first layer. The Ge occupation probability is high (60%–80%) at the surface level and quickly decreases right from the second layer. For a 1 ML Ge deposit, the obtained values are similar to those deduced from a theoretical calculation at 600 °C.[40] The values of the dimer bond length and buckling angle are displayed in Fig. 8.

The complete model with 32 displacements was also tested, but no significant improvement was observed. Moreover, the additional displacements were found to be negligible, and the other displacements were basically unchanged. This validates the 20 displacement model and confirms the vertical symmetry axis at $x = 0.5$.

To conclude, a model of the atomic displacements and the Ge occupation probability of the WL is proposed for 1, 2, and 3 ML coverage. The dimer bond length and buckling angle were then deduced from the displacements. The use of BM32 was appropriate for measuring the ×2 reconstruction peaks.

C. 2 × *N* reconstruction of 2 ML Ge/Si(001)

1. Qualitative analysis and model presentation

Because of the inherent vacancy structure and long period of the ×*N* reconstruction, its diffraction rods are not only much weaker than those of the ×2 reconstruction, but most of them are negligible, i.e., below the background. This was confirmed by many line scans performed on both BM32 and ID03 beamlines. For instance, Fig. 11 compares a radial scan along the $(hh0)_b$ direction for 2 ML Ge coverage measured at BM32 and at ID03. On BM32, only the first-order ×*N* reconstruction rods on the left side of the CTRs (i.e., at $h =$ integer$-1/N$, $h = 0.89$ and 1.89 in this case) were visible above the background, while on ID03, some of the higher-order rods were also measurable (typically those at $h =$ integer$-2/N$, integer$+1/N$, and sometimes integer$+2/N$) thanks to the 20-fold gain in intensity.

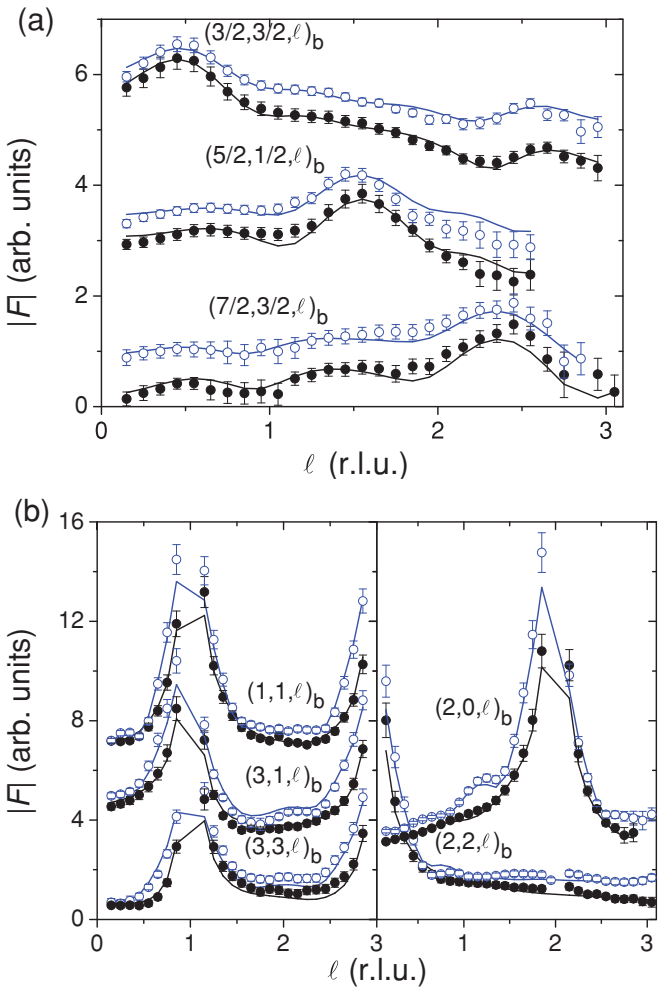

FIG. 9. (Color online) Measured structure factor moduli vs index ℓ of (a) reconstruction rods and (b) CTRs for 1 (filled black circle) and 3 ML (open blue circle) coverage. The continuous lines are the theoretical values.

Using ID03, all k lines at h constant (integer or half-integer) were performed to look for reflections. A total of 113 independent in-plane reconstruction reflections were experimentally confirmed to be below the background. The remaining visible reflections underwent a careful selection that reduced the total number of suitable reflections from 73 to 38 by keeping only the reflections that yielded reasonable and consistent FWHM from both radial and rocking scans. These 38 reflections were further reduced to 19 due to symmetry. In addition, a total number of 193 out-of-plane reflections were measured, which was reduced to 112 nonequivalent intensities corresponding to seven rods [(0.889,0,ℓ), (0.889,0.5,ℓ), (1.889,0,ℓ), (1.889,0.5,ℓ), (1.889,1,ℓ), (1.889,1.5,ℓ), and (2.889,0.5,ℓ)] with a systematic error of 0.09. The rods were measured up to a maximum value $\ell = 2.30$.

The starting model to analyze the 2×9 reconstruction of the 2 ML Ge/Si(001) WL was the structure averaged over y deduced from the above-described analysis of the $\times 2$ reflections. The surface unit cell of the 2×9 reconstruction has two atoms in each plane along the x direction, nine along the y direction (eight for the surface layer), and six planes along the z direction due to intermixing. Hence, the total number of

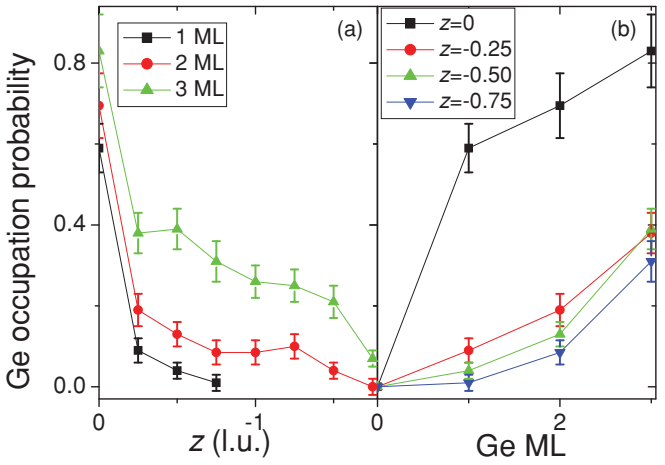

FIG. 10. (Color online) Ge occupation probability (a) for 1, 2, and 3 ML Ge/Si(001) as a function of z and (b) in each of the top four atomic layers ($z = 0, -0.25, -0.50, -0.75$) as a function of the Ge coverage.

atoms is 106. Each atom is defined by its position (xyz) and its Ge (or Si) occupation probability. Hence, a full description of this system calls for 424 parameters. As the number of available data was far from sufficient for a standard structure refinement, we resorted to a simpler model that is inspired by a MC simulation.[24] For 2 ML Ge on Si(001), the simulation showed that the evolution of the atomic displacements as a function of y is a smooth function and could be thus easily accounted for by a low-order polynomial. In our model, each displacement is described by a third-order polynomial as a function of y, multiplied by a decreasing exponential function as a function of z.

Taking into account the cell middle symmetry plane (cf. Fig. 1), the z displacement within each atomic layer is modeled by an even function with respect to this symmetry plane:

$$dz = [b_0 + b_2(y - \bar{y})^2]e^{b_4 \times z} + d_{z0}, \quad (4)$$

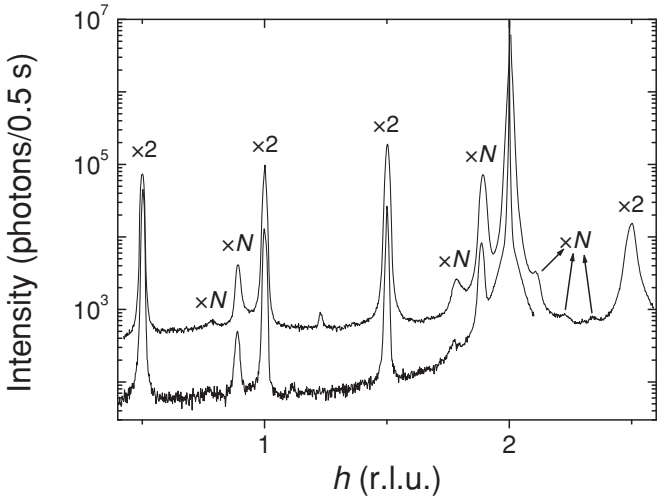

FIG. 11. Measured intensity (logarithmic units) during a radial scan along the $(hh0)_b$ direction for 2 ML Ge coverage measured at BM32 (bottom curve) and at ID03 (top curve).

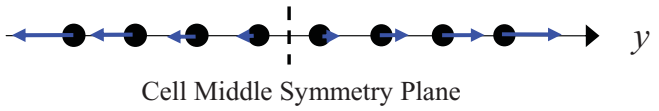

FIG. 12. (Color online) Schematic representation of the atoms in the first layer. The arrows indicate the y displacements.

where $\bar{y}$ is the y position of the atom in the cell middle symmetry plane and d_{z0} is the displacement found for the 2×1 reconstruction. Fitting the z displacements thus requires three parameters.

Along the y axis, the MC simulation showed that the distance between neighboring dimers increases significantly near the DVL.[24] The closer the atoms are from the DVL, the larger is the absolute value of their displacement from their $\times 2$ reconstruction origin (cf. Fig. 12). The y displacement for atoms in a same layer is thus antisymmetric with respect to the cell middle symmetry plane and is modeled by an odd function. Similar to the precedent case (dz displacement), fitting the dy displacement requires three parameters:

$$dy = [c_1(y - \bar{y}) + c_3(y - \bar{y})^3]e^{c_4 \times z}. \quad (5)$$

Initially, a polynomial had been introduced also along the x axis, but all displacements happened to be very small and ill-defined. A qualitative study was thus undertaken with only two parameters (see below).

Taking into account the cell middle symmetry plane, the Si (Ge) θ_{occ} occupation probability was modeled by an even function with respect to this symmetry plane,

$$\theta_{\text{occ}} = d_0 + [d_2(y - \bar{y})^2]e^{d_4 \times z}. \quad (6)$$

Note that the d_0 parameter varies with the atomic layer. Fitting the occupancies thus requires eight additional parameters.

In all, 131 quantitatively measured structure factors (19 in-plane and 112 out-of-plane) were fitted with 17 parameters (three for z, three for y, two for x, eight for θ_{occ}, and an overall scale factor). This yields a rather reasonable factor of approximately eight reflections per parameter. However, a reduced set of parameters usually implies an increase in their correlations. These correlations were partially taken into account by calculating the error bars with the covariance matrix.[37] The best fit yields the z and y atomic displacement as a function of y and z.

2. *Best-fit results*

A total of ten parameters (three for y, six d_0 parameters for θ_{occ}, and an overall scale factor) were initially refined using the 19 in-plane structure factors. The θ_{occ} evolution was only obtained at the end along with other out-of-plane parameters, since it contributes relatively less to the overall structure factor. The corresponding error bars were evaluated following the same order. For the in-plane measurements, the best fit of the structure factors ($\chi^2 = 2.35$) is displayed in Fig. 13.

Below-background diffractions were recorded at the location where intensities calculated with the model are very weak. This good agreement between experimental and calculated intensities accounts for 113 independent reflections.

For the out-of-plane measurements, the best fit of the structure factors ($\chi^2 = 1.51$) is displayed for four rods

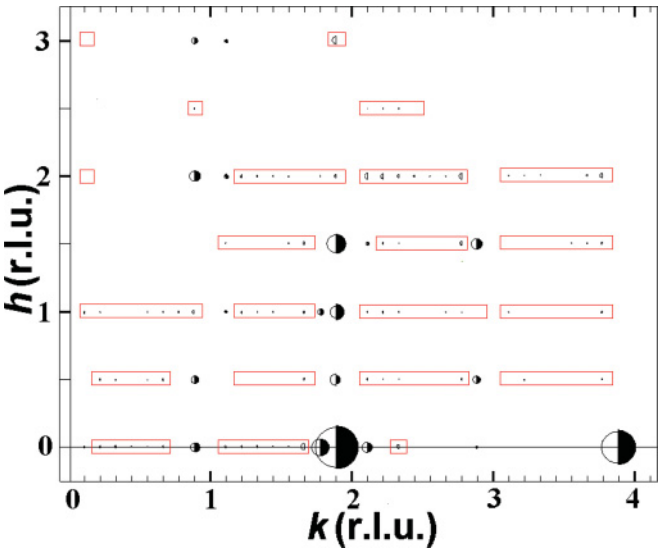

FIG. 13. (Color online) Top view of the in-plane diffraction pattern. The measured reflections are drawn as right black half-disks of radius (area) proportional to the structure factor amplitude (intensity). The left half-circles represent the fitted structure factors according to the model. The confirmed below-background diffractions are surrounded by the rectangles. Corresponding values calculated with the model are also drawn. The h and k indexes are those of the unreconstructed surface unit cell $(1 \times 1)_s$.

[(0.889,0,ℓ), (0.889,0.5,ℓ), (1.889,0,ℓ), and (1.889,1.5,ℓ)] in Fig. 14. The overall agreement is good, supporting the idea that the model should not be far from the real situation.

The z displacements with respect to the initial values of the 2×1 reconstruction are shown in Fig. 15. In each layer, the atoms close to the DVL symmetry plane are found to have the largest vertical motions.

The relative uncertainty on the z atomic displacement can be estimated by $\Delta(dz)/dz = \Delta b_4 \times z$, as the uncertainties on the fit parameters b_0 and b_2 in Eq. (4) are negligible with

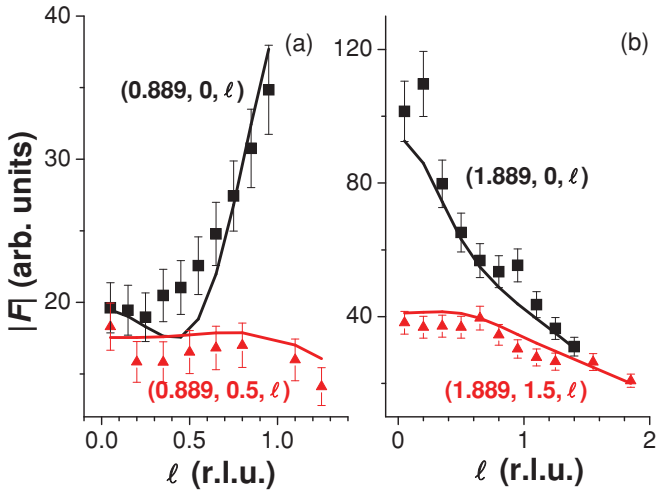

FIG. 14. (Color online) Experimental structure factors for four measured rods vs index ℓ: (a) (0.889,0,ℓ) and (0.889,0.5,ℓ), (b) (1.889,0,ℓ) and (1.889,1.5,ℓ). The lines correspond to the best fits with the chosen model.

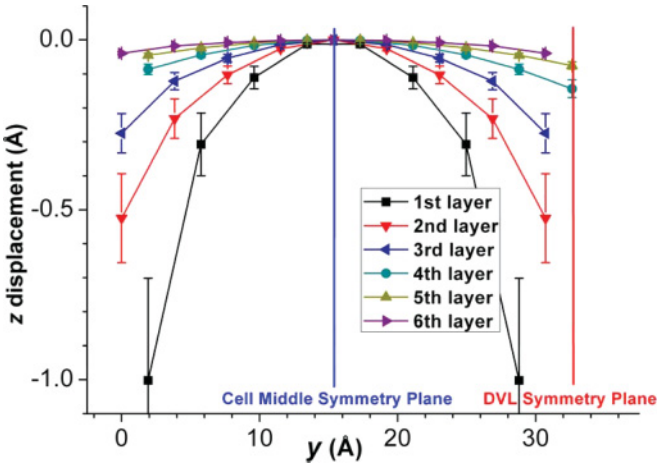

FIG. 15. (Color online) The z atomic displacement with respect to the initial values of the 2×1 reconstruction for 2 ML coverage in layers (1) to (6).

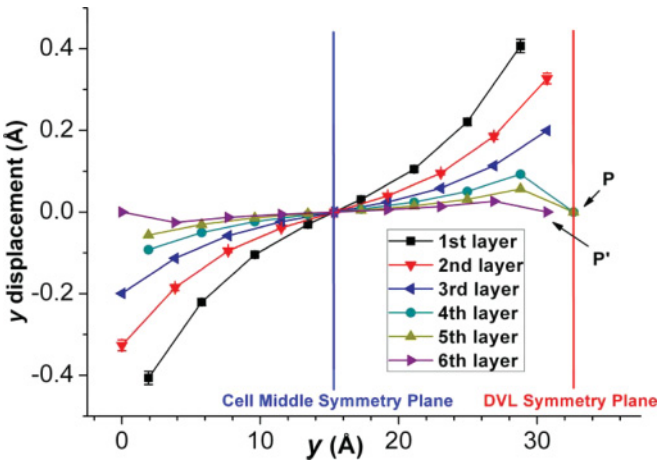

FIG. 16. (Color online) The y atomic displacement in layers (1) to (6) for 2 ML coverage. Most error bars are smaller than the symbol size.

respect to that of b_4 ($\Delta b_4/b_4 \sim 5\%$). Hence, the uncertainties are approximately 30% for the first layer, 25% for the second layer, 21% for the third layer, 18% for the fourth layer, 14% for the fifth layer, and 10% for the sixth layer, decreasing linearly with depth.

The y displacement is displayed in Fig. 16. Again, in each layer, the largest displacements are undergone by the atoms closest to the DVL symmetry plane. The atoms indicated as P in layers (4) and (5) in Fig. 16 do not move along y as they are in the DVL symmetry plane. Moreover, these atoms move down along z (cf. Fig. 15) and prevent the atom indicated as P' in the layer (6) to move along y (cf. Fig. 16).

The uncertainty on the y atomic displacement can be estimated by $\Delta(dy)/dy = \Delta c_4 \times z$, as the uncertainties on the c_1 and c_3 parameters in Eq. (5) are negligible with respect to that of c_4 ($\Delta c_4/c_4 \sim 1.2\%$). Hence, the uncertainties on the y atomic displacement are around 5% for the first layer, 4% for the second and third layers, 3% for the fourth layer, and 2% for the fifth and sixth layers.

A preliminary polynomial modelization revealed that the x displacements of most atoms are negligible with respect to their original positions in the $\times 2$ reconstruction. Hence, a qualitative study was carried out specifically on the two atoms in layer (2) near the DVL where the x displacements are expected to be the largest. The study showed that these two atoms (cf. Fig. 17) tend to move slightly away from each other from their initial positions in the $\times 2$ reconstruction, thus partially compensating the compressive strain induced by the large z displacement of their nearest neighbor in layer (1).

The best fit also yields the average Ge occupation probability with reasonable uncertainties (cf. Table II).

The evolution of the Ge occupation probability is displayed in Fig. 18 for layers (3), (4), and (5). The SXRD shows that, from layer (3), the Ge occupation decreases from the cell middle symmetry plane to the DVL one. However, no such variation was found for layers (1) and (2).

To conclude, the available x-ray data are well fitted with the chosen model. The best fits yielded the z and y atomic displacement as a function of y and z, as well as the Ge occupation probability in each atomic layer by using 17 parameters.

IV. DISCUSSION

A. Asymmetric dimer bond lengths and buckling angles

The best fits of the 2×1 reconstruction for Si and 1, 2, and 3 ML Ge/Si(001) confirm the dimer asymmetry. Let us compare the deduced dimer bond length and buckling angle (cf. Fig. 8) with those found in the literature. Previous SXRD measurements of the Si(001) reconstruction yielded a bond

TABLE II. Average Ge occupation probability in each atomic layer for 2 ML Ge/Si(001) WL grown at 670 °C, obtained from the present SXRD study. For comparison, the average Ge occupation probabilities obtained from MC simulations at 600 °C are also reported.[24] In this case, the intermixing region covers layers 1–5 or the whole bulk region (see Sec. IV for discussion).

		MC	
Layer	SXRD	Intermixing in five layers	Intermixing in the whole bulk
1	79.6% ± 8%	91%	66%
2	49.3% ± 12%	33.5%	10%
3	14.7% ± 21%	26%	8%
4	14.2% ± 27%	24.5%	8%
5	11.7% ± 28%		
Sum	1.70 ML	1.75 ML	0.92 ML

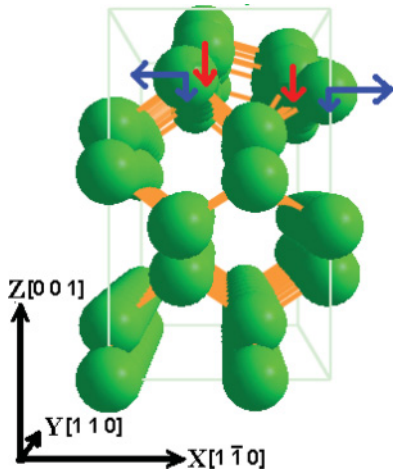

FIG. 17. (Color online) Schematic of the 2 × 9 reconstruction for 2 ML coverage. The arrows show the displacements of the atoms in the second layer and the *z* displacements of the dimer atoms near the DVL.

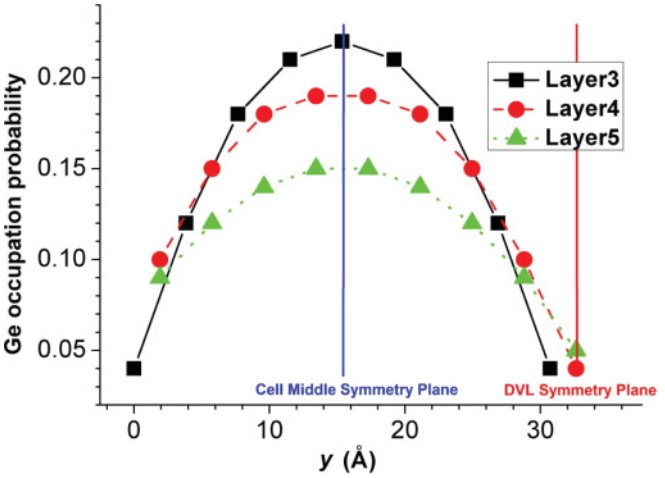

FIG. 18. (Color online) Ge occupation probability as a function of *y* for layers (3), (4), and (5) for 2 ML coverage. The uncertainties on the Ge occupation probability within a layer are large (typically 80% for the fifth layer).

length of 2.67 ± 0.07 Å and a buckling angle of 20° ± 3°.[39] Another SXRD study of the Ge(001) reconstruction indicated a bond length of 2.55 ± 0.01 Å and a buckling angle of 15.6° ± 0.6°.[34] X-ray standing-wave measurements of 1 ML Ge/Si(001) determined a bond length of 2.60 ± 0.04 Å and a buckling angle of 12.1° ± 0.2°.[9] A first-principles local-density molecular-cluster total-energy and atomic-force study of Ge dimers on Si(001) yielded a buckling angle of 14.2°.[11] In addition, final-state pseudopotential theory for 1 ML Ge/Si(001) gave a buckling angle of 16°.[41] Globally, the buckling angles deduced from the present SXRD measurements (between 9.4° and 15.6° depending on Ge coverage) are in good agreement with those found in the literature. Surface-extended x-ray-absorption fine structure indicated that the bond length is 2.51 ± 0.04 Å for 1 ML Ge/Si(001).[42] Furthermore, first-principles total-energy calculations yielded a bond length of 2.54 Å for a $p(2 \times 2)$ reconstruction for 1 or more ML coverage.[15] Another first-principles study of 1 ML Ge/Si(001) in the $p(2 \times 2)$ reconstruction found a bond length of 2.55 Å.[43] X-ray diffraction of the $c(4 \times 2)$ reconstruction of Ge(001) at 150 K yielded a bond length of 2.55 Å.[44] The calculated bond length using a (4 × 2) unit cell is 2.51 Å.[45] Globally, the bond lengths obtained by SXRD for the 1, 2, and 3 ML coverage (between 2.5 and 2.62 Å depending on coverage) are also in good agreement with those experimentally determined or calculated for alternating asymmetric dimers. This indicates that the alternating asymmetric dimers correspond to the most stable structure. The calculated bond lengths for a (4 × 2) unit cell are longer than those calculated for a (2 × 1) symmetry,[46,47] showing that the bond length depends strongly on the long-range interaction between dimers or on the surface stress extending over several dimer units.

More precisely, the measured bond lengths (buckling angles) of the 1 and 2 ML Ge/Si(001), displayed in Fig. 8, are smaller (larger) than those of clean Si and of 3 ML Ge/Si(001). For 3 ML coverage, since the Ge occupation probability is larger than 80%, most dimers are Ge-Ge dimers, while for low coverage, mixed Si-Ge dimers are favored.[10] Hence, the present SXRD study confirms that the buckling angle of a Si-Ge dimer is significantly larger than that of a pure Si dimer.[12] In addition, our results show that the buckling angles of mixed dimers are also larger than those of pure Ge dimers. As a matter of fact, the surface total-energy reduction due to the buckling of the dimers has been evaluated to 0.13 eV/dimer for the Si-Si dimer,[13] 0.28 eV/dimer for the Si-Ge dimer,[13] and 0.13 eV/dimer for the Ge-Ge dimer.[11] Therefore, the buckling of the mixed dimer is energetically the most favorable process. This can be attributed to the strain relief of the dimers, which reduces the strain energy of the surface, as the lattice constant of Ge is larger than that of Si. Since Ge is coherent with the Si(001) substrate, a tetragonal distortion of the Si-Ge dimers along the [001] direction reduces the strain in the Ge/Si(001) interfaces. In short, the bond length of Si-Ge dimers is smaller (∼2.50 Å) than those of pure Si or pure Ge dimers, while the buckling angle of mixed dimers is larger (∼16°). This structural difference comes from the strain associated with the lattice mismatch between Si and Ge.

B. The DVL × *N* reconstruction

The average *N* value is found to decrease from 11.5 to 8 with increasing Ge coverage from 1 to 3 ML. This value is in good agreement with previous theoretical and experimental studies. A MC simulation shows that, in the absence of intermixing (e.g., at low growth temperatures), *N* first decreases with increasing coverage and then saturates at $N = 8$ at approximately 2 ML coverage.[24] Taking into account intermixing, the calculated *N* value shifts from 8 to larger values for 2 ML coverage and $N \sim 8$ for 3 ML coverage.[24] Moreover, a high-temperature STM study showed that *N* decreases from 10 for 1.2 ML coverage to 8–9 for 2 ML coverage.[48]

Besides, the intermixing depth is found to increase from six to eight layers with increasing Ge coverage from 2 to 3 ML. This is also in good agreement with previous theoretical and experimental studies. The MC method shows that at

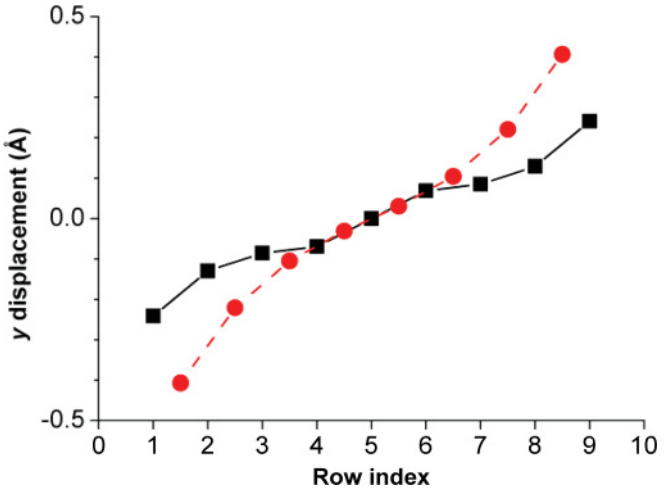

FIG. 19. (Color online) Evolution of the y displacement in the first layer as a function of the dimer line index. The y displacement of the 2×9 reconstruction obtained from the present SXRD data is represented by filled circles and the one from a theoretical study for a 2×10 reconstruction without intermixing at $T = 11$ K is represented by filled squares.[24] The uncertainty on the experimental y displacement for the first layer is 4%.

600 °C, a significant Ge amount is present throughout the surface region, with the third and fourth layers becoming populated even at low coverages.[24] Previous experiments showed that Ge is present at least in the fourth layer for monolayer or even submonolayer deposits.[49–52]

Regarding the atomic displacements of the $2 \times N$ reconstruction, the obtained y displacement in the first layer is plotted together with that calculated in an MC simulation for a 2×10 reconstruction without intermixing at $T = 11$ K in Fig. 19. [24] The evolution of both curves is similar, i.e., the y displacement in absolute value increases from the middle of the lattice toward the DVL. Interestingly, near the DVL, the y displacement obtained for the 2×9 reconstruction is larger than the theoretical one for the 2×10 reconstruction. This can probably be attributed to the fact that the DVLs act as a misfit strain relief mechanism by providing space for the expansion of the Ge-rich overlayer. This effect is expected to be larger for a DVL every ninth line than for a DVL every tenth line. In addition, the atomic displacements may be larger at RT (current study) than at $T = 11$ K (MC simulation).[24]

The average Ge occupation probability at 2 ML coverage is shown in comparison (Table II) with theoretical results.[24] The experimental average Ge occupation probability is similar to that obtained from the MC simulations. More precisely, SXRD shows that the Ge occupation probability is maximum in the middle of the lattice and minimum near the DVLs below the surface from the third layer (cf. Fig. 18). This site selectivity agrees well with a MC simulation that shows that the region under the DVL is unfavorable to Ge occupation.[24] Indeed, the inward relaxation leads to a compressively strained region near the DVL that becomes unfavorable to Ge occupation. The site selectivity is due to the strain coming from the lattice mismatch between Si and Ge. Finally, the atomic structure of the 2×9 reconstruction with the effect of the DVL is schematically represented in Fig. 20.

Last but not least, the literature suggests that a small disturbance in the WL locally modifies the strain configuration, leading to the formation of prepyramids.[53] Our results suggest that the top of the Ge-rich region might be a preferable site for island nucleation due to larger strain relief for Ge atoms.

V. CONCLUSION

The $2 \times N$ reconstruction of the Ge/Si(001) WL was investigated by SXRD for Ge coverages between 1 and 3 ML.

The structure of its cornerstone, the surface dimers, was first studied. The buckling angle was found between 9.4° and 15.6° and the dimer bond length was between 2.50 and 2.60 Å depending on the coverage. The bond lengths correspond to those calculated for alternating asymmetric dimers, which are smaller than those of pure Si and pure Ge dimers, while the buckling angles are larger. These results suggest that a significant proportion of the dimers are mixed dimers.

The overall $2 \times N$ reconstruction was then investigated. The average N periodicity is found to decrease from 11.5 to 8 with increasing Ge coverage from 1 to 3 ML. Intermixing is found to extend below the surface down to six (eight) layers for 2 (3) ML coverage.

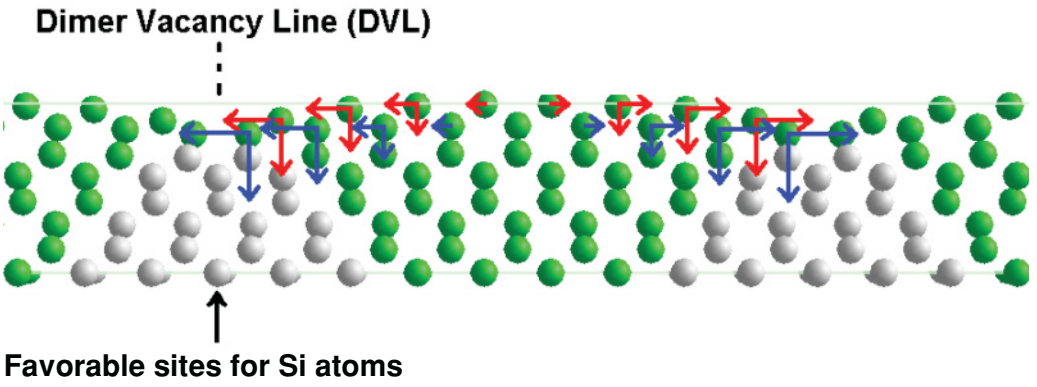

FIG. 20. (Color online) Schematic representation of the atomic structure of the 2×9 reconstruction. The red (gray) [blue (dark)] arrows indicate the displacements of the atoms in layer (1) [(2)]. Lattice sites that are under tensile strain and thus richer in Ge atoms are represented by green (dark gray) disks. Sites under compression and thus richer in Si atoms are represented by light gray disks.

For 2 ML coverage, a model of the atomic displacements and the Ge occupation probability for the 2×9 reconstruction is proposed. The largest displacements are located below the DVLs, with a smooth decrease with increasing distance from the DVLs. The average Ge occupation probability decreases from approximately 80% in the first layer down to 12% in the fifth layer. An experimental proof for the site selectivity in intermixing is also provided, which reveals that the regions under the DVLs are unfavorable to Ge. The top of the Ge-rich region between the DVLs might then be a preferable site for prepyramid nucleation. The intermixing in the WL may be responsible for the observed intermixing in the prepyramids and pyramids that form at the 2D-3D transition, atomic motion being favored by the stress present in the wetting layer, especially in the Si-richer regions below the DVLs.

ACKNOWLEDGMENTS

We would like to thank D. Vermeille of the ESRF ID03 beamline for his invaluable help during the measurements. We would also like to thank D. Hauser for his help in analyzing the SXRD data, and C. Metzig for guiding Monte Carlo simulations. The 2×9 reconstruction was displayed with V_Sim, a free 3D visualization tool available at [http://inac.cea.fr/L_Sim/V_Sim/]. We acknowledge support by the University Joseph Fourier, Grenoble, France, with which the SP2M laboratory is associated.

APPENDIX

A. Lorentz factor

The differential scattering cross section is expressed in reciprocal space as the integration is performed on the scan angles. The Lorentz factor is a geometrical correction factor whose value is equal to the determinant (also called Jacobian) of the transformation matrices between both volumes. The Lorentz factor for a rocking scan is given, for example, in Ref. 31. This factor is calculated here with another approach. Once this approach is validated for a rocking scan, it will be used for a radial scan for which the Lorentz factor is rarely given.

In the case of a rocking scan, the integration volume V expressed in terms of angles is given by[31]

$$V = (K_f \mathrm{d}\boldsymbol{\psi} \times K_f \mathrm{d}\boldsymbol{\gamma}) \cdot \mathrm{d}\mathbf{Q} = K \mathrm{d}\psi \, K \mathrm{d}\gamma \cos\gamma \, \mathrm{d}Q_{\parallel}^{*}, \quad \text{(A1)}$$

where $\mathbf{Q} = \mathbf{K}_f - \mathbf{K}_i$ is the momentum transfer, $K = K_i = K_f$ is the wave-vector value, and $\mathrm{d}Q_{\parallel}^{*}$ is the component of $\mathrm{d}\mathbf{Q}$ parallel to the direction of $\mathbf{K}_f$. The $\mathrm{d}Q_{\parallel}^{*}$ parameter can be expressed as

$$\mathrm{d}Q_{\parallel}^{*} = \mathrm{d}\mathbf{Q}_{\parallel}^{*} \cdot \frac{\mathbf{K}_{f\parallel}}{K_{f\parallel}} = \mathrm{d}Q_{\parallel} \sin\tau = Q_{\parallel} \mathrm{d}\omega \, \sin\tau, \quad \text{(A2)}$$

where τ is the angle between $\mathbf{Q}_{\parallel}$ and $\mathbf{K}_{f\parallel}$. Let us now compare two expressions of the surface A of the triangle O-S'-P' in Fig. 21:

$$S = \frac{1}{2} Q_{\parallel} K_{f\parallel} \sin\tau = \frac{1}{2} K_{i\parallel} K_{f\parallel} \sin\delta \Leftrightarrow \sin\tau = \frac{K_{i\parallel} \sin\delta}{Q_{\parallel}} = \frac{K \cos\alpha \sin\delta}{Q_{\parallel}}. \quad \text{(A3)}$$

Hence, one obtains

$$V = K \mathrm{d}\psi \, K \mathrm{d}\gamma \cos\gamma \, Q_{\parallel} \mathrm{d}\omega \frac{K \cos\alpha \sin\delta}{Q_{\parallel}} = K^3 \cos\alpha \sin\delta \cos\gamma \, \mathrm{d}\psi \, \mathrm{d}\gamma \, \mathrm{d}\omega, \quad \text{(A4)}$$

which is the expression given in the literature for an in-plane rocking scan (i.e., ω scan).[31]

For a radial scan, the calculation is similar except that the scan direction is along $\mathbf{Q}_{\parallel}$. The integration volume can be described as

$$V = K \mathrm{d}\psi \, K \mathrm{d}\gamma \cos\gamma \, \mathrm{d}Q_{\parallel}^{**} \quad \text{(A5)}$$

with

$$\mathrm{d}Q_{\parallel}^{**} = \mathrm{d}\mathbf{Q}_{\parallel}^{**} \cdot \frac{\mathbf{K}_{f\parallel}}{K_{f\parallel}} = \mathrm{d}Q_{\parallel} \sin\left(\frac{\pi}{2} - \tau\right) = \mathrm{d}Q_{\parallel} \cos\tau. \quad \text{(A6)}$$

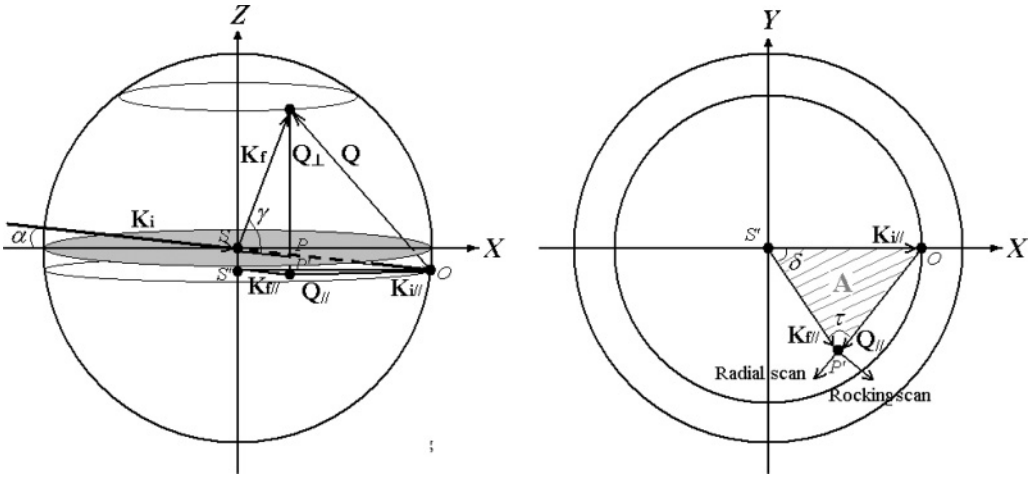

FIG. 21. Construction of the Ewald sphere for the z-axis diffractometer geometry.

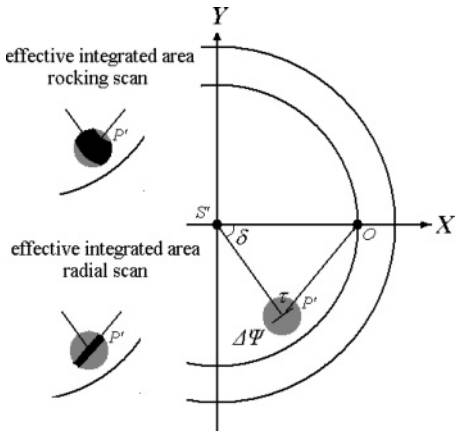

FIG. 22. Construction of the Ewald sphere (top view of the surface plane) for the z-axis diffractometer geometry and effective integrated area for a rocking scan or a radial one.

The law of cosines is next applied (for the same triangle as before in Fig. 21) to get an analytical expression,

$$Q_{\parallel}^2 = K^2\cos^2\gamma + K^2\cos^2\alpha - 2K^2\cos\alpha\cos\gamma\cos\delta \Leftrightarrow dQ_{\parallel} = \frac{K^2\cos\alpha\cos\gamma\sin\delta}{Q_{\parallel}}d\delta, \quad \text{(A7)}$$

$$K^2\cos^2\alpha = Q_{\parallel}^2 + K^2\cos^2\gamma - 2Q_{\parallel}K\cos\gamma\cos\tau \Leftrightarrow \cos\tau = \frac{Q_{\parallel}^2 + K^2\cos^2\gamma - K^2\cos^2\alpha}{2Q_{\parallel}K\cos\gamma}. \quad \text{(A8)}$$

Finally, the expression for V becomes

$$V = Kd\psi\, Kd\gamma\cos\gamma\frac{K^2\cos\alpha\cos\gamma\sin\delta}{Q_{\parallel}} \times d\delta\frac{2K^2\cos^2\gamma - 2K^2\cos\alpha\cos\gamma\cos\delta}{2Q_{\parallel}K\cos\gamma}, \quad \text{(A9)}$$

and with the help of (A7), a simpler result is obtained:

$$V = K^3 d\psi d\gamma d\delta\frac{\cos\alpha\sin\delta\cos^2\gamma(\cos\gamma - \cos\alpha\cos\delta)}{\cos^2\gamma + \cos^2\alpha - 2\cos\alpha\cos\gamma\cos\delta}. \quad \text{(A10)}$$

B. Detector acceptance

The square of the structure factor is proportional to the integrated intensity of the corresponding peak. However, the angular acceptance of the detector may not be large enough in certain cases. For example, when the surface is not well organized, the FWHM of the peaks can be extremely large. It is often possible to perform a very wide scan so that along the scan direction, the peak can be fully integrated. On the contrary, the integration along the other direction (perpendicular to the scan direction) is still limited by the detector angular acceptance. Figure 22 illustrates the effective integrated area of a wide peak during a rocking scan or a radial scan when the detector angular acceptance cannot be made large enough. When this happens, an additional correction factor has to be applied, equal to the ratio between the effective integrated intensity and the entire peak intensity. For in-plane data sets, an analytical correction factor for a rocking scan is given for a Lorentzian or Gaussian line shape in the literature. For a general setting, a numerical correction factor is given for a rocking scan but not for a radial scan.[31]

Let us derive an analytical correction factor for a more general setting. A much simpler calculation using the τ angle will be described later. First, consider the common case of a two-dimensional Lorentzian line shape, for which

$$I = \int_{-\infty}^{+\infty}\int_{-\infty}^{+\infty} f_{\mathrm{Lor}}(x,y;x_0,y_0,w)dx\,dy = \int_{-\infty}^{+\infty}\int_{-\infty}^{+\infty}\frac{w}{4\pi}\frac{1}{\left(\frac{w^2}{4} + \Delta x^2 + \Delta y^2\right)^{3/2}}dx\,dy, \quad \text{(A11)}$$

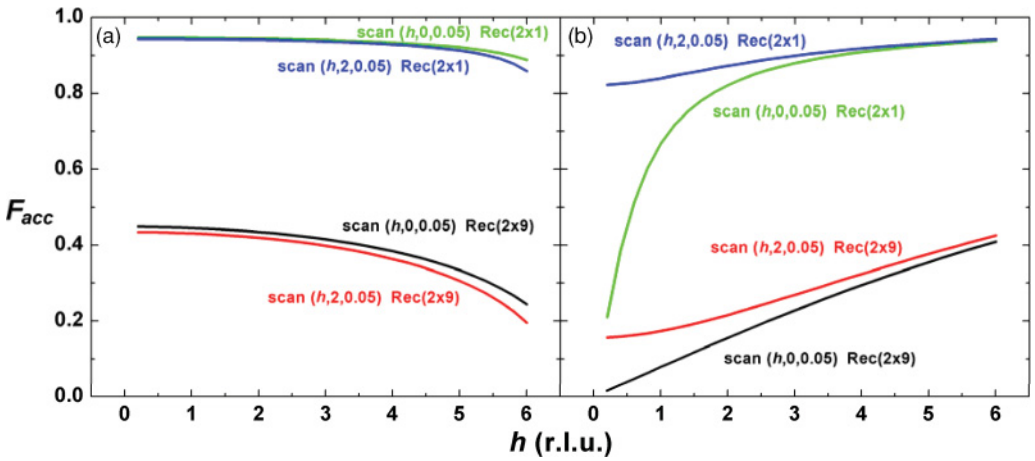

FIG. 23. (Color online) The correction factor of detector acceptance for a Lorentzian line shape in the case of (a) a rocking scan and (b) a radial scan. The parameters are drawn from our case with a horizontal opening angle of the detector $\Delta\Psi = 0.2^\circ$, corresponding to 0.02 Å^{-1} in reciprocal space. The factors for the two surface reconstructions ($\times 2$ and $\times 9$) are presented for two different peaks (h,0,0.05) and (h,2,0.05). The $\times 2$ reconstruction has a typical FWHM of $L_{\times 2} = 1.65 \times 10^{-3}$ Å^{-1} and the $\times 9$ reconstruction has a typical FWHM of 2.3×10^{-2} Å^{-1}, i.e., approximately $14 \times L_{\times 2}$.

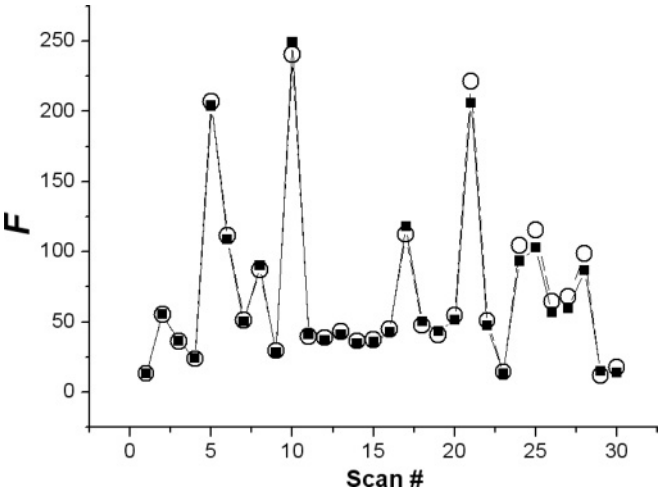

FIG. 24. Comparison of the structure factor after correction for the corresponding rocking (filled squares) and radial (open circles) scans.

where w is the FWHM of the distribution and Δx and Δy denote the deviation from the position of the distribution maximum given by x_0 and y_0. The distribution is two-dimensionally homogeneous so that the integral is the same for two other variables of integration orthogonal to each other: $\mathrm{d}\mathbf{q}_t$ (the transverse component of $\mathrm{d}\mathbf{Q}$) and $\mathrm{d}\mathbf{q}_r$ (the radial component of $\mathrm{d}\mathbf{Q}$). The total integrated intensity is

$$I_{\mathrm{tot}} = \int_{-\infty}^{+\infty}\int_{-\infty}^{+\infty} \frac{w}{4\pi} \frac{1}{\left(\frac{w^2}{4} + \Delta q_t^2 + \Delta q_r^2\right)^{3/2}} \mathrm{d}q_t \mathrm{d}q_r . \tag{A12}$$

In the case of a rocking scan, where the detector moves transversally with respect to $\mathbf{Q}$, the integral interval over $\mathrm{d}q_t$ can have the maximum value while the one over $\mathrm{d}q_r$ depends on the effective length of the detector slit ($L_{\mathrm{eff}} = 2T$), which is perpendicular to the scan direction. The effective integrated intensity is thus

$$I_{\mathrm{eff}} = \int_{-T}^{+T}\int_{-\infty}^{+\infty} \frac{w}{4\pi} \frac{1}{\left(\frac{w^2}{4} + \Delta q_t^2 + \Delta q_r^2\right)^{3/2}} \mathrm{d}q_t \mathrm{d}q_r . \tag{A13}$$

The detector acceptance correction factor acceptance is then the quotient of both integrated intensities:

$$F_{\mathrm{acc}} = I_{\mathrm{eff}}/I_{\mathrm{tot}} = \frac{2}{\pi} \arctan\left(\frac{2T}{w}\right). \tag{A14}$$

For a radial scan, the expression of the factor is the same as in formula (A13) while the value of the effective length $L_{\mathrm{eff}} = 2T$ is different because it is now the integral over $\mathrm{d}q_t$, which is limited. By calculating L_{eff} for both cases, we obtain

$$2T = \frac{L_{\mathrm{oslit}}}{D_{\mathrm{sample\,detector}}} K_f \times \begin{cases} \sin\tau, & \text{rocking scan} \\ \cos\tau, & \text{radial scan,} \end{cases} \tag{A15}$$

where we can replace directly the part related to τ with the expression given in formulas (A3) and (A7), respectively. A similar calculation can also be done for a Gaussian line shape.

The detector acceptance correction factors for rocking and radial scans are shown in Fig. 23. For a rocking scan, let us consider that most data are measured at $h < 4$. The correction factor can be thought to be constant (0.93) for the 2×1 reconstruction. Neglecting the correction factor results only in a slight constant underestimation of the structure factor, easily taken into account by the overall scale factor. For the $\times 9$ reconstruction, only about 40% of the peak would be integrated, nevertheless neglecting the same factor would cause a variation of up to 20% throughout the in-plane data set.

For a radial scan, the factor becomes crucial even for the 2×1 reconstruction. In an extreme case, such as the $(h,0,0.05)$ scan, the correction factor increases dramatically from 20% for $h = 0.2$ (because at small $|\mathbf{Q}|$, the detector is practically parallel to the radial direction) to 91% for $h = 4$. For the $\times 9$ reconstruction, the factor changes linearly with h. Even in the best cases [i.e., $(h,2,0.05)$], neglecting the correction factor would cause a variation of up to 50% throughout the in-plane data set.

Finally, Fig. 24 shows that both kinds of measurements (rocking and radial scans) yield the same structure factor amplitude after corrections, thus validating the corrections applied in this work.

[1] B. Voigtländer, Surf. Sci. Rep. **43**, 127 (2001).
[2] Y. W. Mo, D. E. Savage, B. S. Swartzentruber, and M. G. Lagally, Phys. Rev. Lett. **65**, 1020 (1990).
[3] A. Vailionis, B. Cho, G. Glass, P. Desjardins, D. G. Cahill, and J. E. Greene, Phys. Rev. Lett. **85**, 3672 (2000).
[4] G. Medeiros-Ribeiro, A. M. Bratkovski, T. I. Kamins, D. A. A. Ohlberg, and R. S. Williams, Science **279**, 353 (1998).
[5] M.-I. Richard, T. U. Schülli, G. Renaud, E. Wintersberger, G. Chen, G. Bauer, and V. Holý, Phys. Rev. B **80**, 045313 (2009).
[6] T. U. Schülli, J. Stangl, Z. Zhong, R. T. Lechner, M. Sztucki, T. H. Metzger, and G. Bauer, Phys. Rev. Lett. **90**, 066105 (2003).
[7] S. Miyamoto, O. Moutanabbir, E. E. Haller, and K. M. Itoh, Phys. Rev. B **79**, 165415 (2009).
[8] T. U. Schülli, M.-I. Richard, G. Renaud, V. Favre-Nicolin, E. Wintersberger, and G. Bauer, Appl. Phys. Lett. **89**, 143114 (2006).
[9] E. Fontes, J. R. Patel, and F. Comin, Phys. Rev. Lett. **70**, 2790 (1993).
[10] L. Patthey, E. L. Bullock, T. Abukawa, S. Kono, and L. S. O. Johansson, Phys. Rev. Lett. **75**, 2538 (1995).
[11] S. Tang and A. J. Freeman, Phys. Rev. B **50**, 10941 (1994).
[12] X. Chen, D. K. Saldin, E. L. Bullock, L. Patthey, L. S. O. Johansson, J. Tani, T. Abukawa, and S. Kono, Phys. Rev. B **55**, R7319 (1997).
[13] R. H. Miwa, Surf. Sci. **418**, 55 (1998).

[14]H. J. W. Zandvliet, Rev. Mod. Phys. **72**, 593 (2000).
[15]K. Varga, L. G. Wang, S. T. Pantelides, and Z. Zhang, Surf. Sci. Lett. **562**, L225 (2004).
[16]A. van Houselt, R. van Gastel, B. Poelsema, and H. J. W. Zandvliet, Phys. Rev. Lett. **97**, 266104 (2006).
[17]X. R. Qin, B. S. Swartzentruber, and M. G. Lagally, Phys. Rev. Lett. **85**, 3660 (2000).
[18]Z.-Y. Lu, F. Liu, C.-Z. Wang, X. R. Qin, B. S. Swartzentruber, M. G. Lagally, and K.-M. Ho, Phys. Rev. Lett. **85**, 5603 (2000).
[19]F. Liu, F. Wu, and M. G. Lagally, Chem. Rev. **97**, 1045 (1997), and references therein.
[20]R. Gunnella, P. Castrucci, N. Pinto, I. Davoli, D. Sébilleau, and M. De Crescenzi, Phys. Rev. B **54**, 8882 (1996).
[21]J. Wan, Y. H. Luo, Z. M. Jiang, G. Jin, J. L. Liu, K. L. Wang, X. Z. Liao, and J. Zou, J. Appl. Phys. **90**, 4290 (2001).
[22]K. Nakajima, A. Konishi, and K. Kimura, Phys. Rev. Lett. **83**, 1802 (1999).
[23]R. J. Wagner and E. Gulari, Phys. Rev. B **69**, 195312 (2004).
[24]L. Nurminen, F. Tavazza, D. P. Landau, A. Kuronen, and K. Kaski, Phys. Rev. B **68**, 085326 (2003).
[25]I. Goldfarb, J. H. G. Owen, P. T. Hayden, D. R. Bowler, K. Miki, and G. A. D. Briggs, Surf. Sci. **394**, 105 (1997).
[26]M. Tomitori, K. Watanabe, M. Kobayashi, and O. Nishikawa, Appl. Surf. Sci. **76-77**, 322 (1994).
[27]I. K. Robinson and D. J. Tweet, Rep. Prog. Phys. **55**, 599 (1992).
[28]A. Malachias, T. U. Schülli, G. Medeiros-Ribeiro, L. G. Cançado, M. Stoffel, O. G. Schmidt, T. H. Metzger, and R. Magalhães-Paniago, Phys. Rev. B **72**, 165315 (2005).
[29]R. Baudoing-Savois, M. De Santis, M. Saint-Lager, P. Dolle, O. Geaymond, P. Taunier, P. Jeantet, J. Roux, G. Renaud, and A. Barbier, Nucl. Instrum. Methods Phys. Res. B **149**, 213 (1999).
[30]S. Ferrer and F. Comin, Rev. Sci. Instrum. **66**, 1674 (1995).
[31]E. Vlieg, J. Appl. Cryst. **30**, 532 (1997).
[32]O. Robach, Y. Garreau, K. Aïd, and M. B. Véron-Jolliot, J. Appl. Cryst. **33**, 1006 (2000).
[33]G. Renaud, Surf. Sci. Rep. **32**, 1 (1998).
[34]X. Torrelles, H. A. van der Vegt, V. H. Etgens, P. Fajardo, J. Alvarez, and S. Ferrer, Surf. Sci. **364**, 242 (1996).
[35]R. A. Wolkow, Phys. Rev. Lett. **68**, 2636 (1992).
[36]E. Vlieg, J. Appl. Cryst. **33**, 401 (2000).
[37]W. H. Pres, B. P. Flannery, S. A. Teukolsky, and W. T. Vetterling, *Numerical Recipes in C* (Cambridge Univerity Press, Cambridge, 1988).
[38]M. Takahasi, S. Nakatani, Y. Ito, T. Takahashi, X. W. Zhang, and M. Ando, Surf. Sci. **338**, L846 (1995).
[39]R. Felici, I. K. Robinson, C. Ottaviani, P. Imperatori, P. Eng, and P. Perfetti, Surf. Sci. **375**, 55 (1997).
[40]J.-H. Cho and M.-H. Kang, Phys. Rev. B **61**, 1688 (2000).
[41]J.-H. Cho, S. Jeong, and M.-H. Kang, Phys. Rev. B **50**, 17139 (1994).
[42]H. Oyanagi, K. Sakamoto, R. Shioda, Y. Kuwahara, and K. Haga, Phys. Rev. B **52**, 5824 (1995).
[43]J. Oviedo, D. R. Bowler, and M. J. Gillan, Surf. Sci. **515**, 483 (2002).
[44]S. Ferrer, X. Torrelles, V. H. Etgens, H. A. van der Vegt, and P. Fajardo, Phys. Rev. Lett. **75**, 1771 (1995).
[45]Y. Miyamoto, Phys. Rev. B **49**, 1947 (1994).
[46]P. Kruger and J. Pollmann, Phys. Rev. B **47**, 1898 (1993).
[47]J.-H. Cho and M.-H. Kang, Phys. Rev. B **49**, 13670 (1994).
[48]B. Voigtländer and M. Kästner, Phys. Rev. B **60**, R5121 (1999).
[49]M. Sasaki, T. Abukawa, H. W. Yeom, M. Yamada, S. Suzuki, S. Sato, and S. Kono, Appl. Surf. Sci. **82-83**, 387 (1994).
[50]A. Ikeda, K. Sumitomo, T. Nishioka, T. Yasue, T. Koshikawa, and Y. Kido, Surf. Sci. **385**, 200 (1997).
[51]H. W. Yeom, M. Sasaki, S. Suzuki, S. Sato, S. Hosoi, M. Iwabuchi, K. Higashiyama, H. Fukutani, M. Nakamura, T. Abukawa, and S. Kono, Surf. Sci. **381**, L533 (1997).
[52]B. P. Uberuaga, M. Leskovar, A. P. Smith, H. Jónsson, and M. Olmstead, Phys. Rev. Lett. **84**, 2441 (2000).
[53]A. Rastelli, H. Von Känel, B. J. Spencer, and J. Tersoff, Phys. Rev. B **68**, 115301 (2003).